Real-time In-Situ Passive Acoustic Array Beamforming from the AutoNaut Wave-Propelled Uncrewed Surface Vessel

Alfie Anthony Treloar,
Hugh Maclean, Jan Bujalka, Jon Narramore, Ben Thomas, Philippe Blondel,
Alan Hunter, *Senior Member, IEEE*

Abstract

This article presents the first demonstration of beamforming, detection and bearing estimation of an underwater acoustic source from an 8-element thin line hydrophone array towed behind the AutoNaut wave-propelled uncrewed surface vessel. This has been achieved in-situ and in real-time during an experimental sea trial off the coast of Plymouth, UK. A controlled acoustic source was towed from a support vessel while emitting 7 tonals with frequencies between 480–$1630\,\mathrm{Hz}$ and source levels between 93–$126\,\mathrm{dB}$. This allowed the detection performance of the array to be assessed and demonstrated for an acoustic source with known bearing and range. In post-processing, the shape of the array was estimated using a cubic spline model, exploiting measurements from pressure and 3-axis compass sensors integrated at each end of the array. The beamforming was repeated using the estimated array shape to infer the hydrophone positions, which resulted in a median improvement of $0.38\,\mathrm{dB}$ and maximum of $5.8\,\mathrm{dB}$ in the MUSIC beamforming output, and a potential reduction in the left/right bearing estimation ambiguities. The outcomes of this work demonstrate that the AutoNaut is an effective platform for towed array passive acoustic monitoring.

A. Anthony Treloar e-mail: A.O.Anthony.Treloar@bath.ac.uk

A. Anthony Treloar, Philippe Blondel, Ben Thomas and Alan Hunter are with the University of Bath

J. Bujalka and J. Narramore are with Seiche Ltd.

H. Maclean was with AutoNaut Ltd.

Real-time In-Situ Passive Acoustic Array Beamforming from the AutoNaut Wave-Propelled Uncrewed Surface Vessel

I. Introduction

Wave-propelled autonomous vehicles are well suited to persistent marine surveillance applications, due to their low acoustic signature, low visual profile and ability to operate for long durations. Such platforms operate by converting wave-induced motion into forward propulsion and utilizing solar panels to power the sensor payloads. To the best of our knowledge, the two most prominent wave-propelled uncrewed surface vessels (USVs) currently in development and operation are the Wave Glider (made by Liquid Robotics) [1] and the AutoNaut [2]. These vessels both convert wave-induced vertical motion of the surface vehicle directly into forward thrust, using two different designs. The Wave Glider features a sub-surface glider element attached to a surface vessel by a tether, while the AutoNaut is a self-contained surface vehicle utilizing gimbaled hydrofoils at the fore and aft of the vessel. These different morphologies affect the utility of the vessels for various applications, due to differences in ease of vessel deployment and their suitability for integrating different types of sensors. Underwater buoyancy gliders, such as the Slocum [3] and the Seaglider [4], are an alternative platform capable of long-duration missions with low power consumption. These platforms are a class of autonomous underwater vehicle (AUV) that actively alter their buoyancy in order to rise and fall through the water column, converting this vertical motion to horizontal propulsion via wing-like hydrofoils. The resulting sawtooth-like profile gives them a lower horizontal speed than their thruster-equipped conventional counterparts, similarly to wave-propelled vehicles, but they are also capable of significantly higher duration missions. As a sub-surface vehicle they are able to investigate more of the vertical water column, albeit at the expense of real-time connectivity due to the strong attenuation of radiowaves under the water.

Passive sonar is used for a variety of applications involving the detection and localization of underwater sound sources, such as anti-submarine warfare, seismic surveys and marine mammal monitoring. Conventionally, towed arrays have been deployed from large tow ships as the arrays

Fig. 1. A step of the deployment of the digital thin line array behind the AutoNaut USV. After attaching to the stern of the vessel, two operators gradually feed the array into the water from a support vessel.

are cumbersome and are up to multiple kilometers in length. However, the miniaturization of hydrophone technology has allowed uncrewed autonomous tow vessels to be more widely used for this purpose [5], reducing the operational costs and risks for personnel.

Because of the low levels of acoustic emissions of the propulsion systems, wave-propelled vehicles and underwater gliders are ideally suited to deployment of passive acoustic sensors. Underwater gliders equipped with towed arrays have been used successfully to estimate source bearing [6], but more recently hydrophone arrays have been mounted along the leading edge of the wings [7]–[9] or on the nose [10], reducing their interference with the propulsion and simplifying deployment, but limiting their aperture length and angular resolution. The Wave Glider USV has demonstrated the capability to deploy a passive acoustic array [11]–[14] from its sub-surface element, isolating it from surface and mechanical noise. More recently, this has also been achieved for the purpose of real-time marine mammal monitoring [15]. The AutoNaut has also been shown to be capable of array deployment, pictured being deployed in Fig. 1, connected via a vibration isolation module from the stern of the vessel [2], [16], demonstrating the minimal self-noise of the vessel using spectral decomposition of the acoustic data [17]. This basic processing demonstrates the physical capabilities of the vessels, enabling the investigation into the application of more advanced passive sonar techniques.

There are a number of challenges inherent to operating an acoustic array from a wave-propelled vessel and implementing passive acoustic monitoring algorithms on the collected data. Due

to the limited propulsion power of the vessels, the array must have sufficiently low drag to avoid adversely affecting their operation, constraining their length and thickness. The resulting reduced aperture limits the frequencies at which the array can be used to effectively localize a target. For a conventional beamforming algorithm, the half-power beamwidth in degrees of an array of length, L, for frequency, f, is approximately equal to $51c/(fL)$ [18], where c is the propagation speed of sound. Therefore, at low frequencies for short arrays the angular resolution of a beamformed result becomes less usable as closely spaced targets cannot be distinguished. This can potentially be improved through the use of more sophisticated algorithms. However, the inherently intermittent nature and limited speed of wave-propulsion can result in significant deviations from a linear array shape [19], as consistent forward motion through the water typically stabilizes a towed array. This can affect the performance of localization algorithms without array shape compensation, as these algorithms require accurate knowledge of the sensor positions, with errors leading to sub-optimal performance. For example, an error of $\lambda/10$ in the sensor positions will result in a decrease in conventional beamformer gain of $1\,\mathrm{dB}$ [20]. This challenge of compensating for a perturbed array shape has been approached in various different ways, either using acoustic data [21] [22] [23] [24], extrapolating from vessel movement [25] [26], fitting a spline between non-acoustic sensors [27] [28], or some combination of these [29].

This paper presents an experimental investigation into the use of passive acoustic monitoring techniques from an AutoNaut USV. The two main novel contributions are the development and demonstration of a real-time onboard beamforming and detection payload operated from the AutoNaut, and the post-processing investigation into the use of array shape estimation for improvement of these results. The outline of this paper is as follows: Section II details the implemented processing techniques for bearing estimation, detection and array shape estimation; Section III describes the software for real-time processing; Section IV describes the experimental trial from which the data came, along with the hardware involved; and finally Section V presents the results of each stage of the work.

II. Signal and Data Processing

An array of hydrophones provides the ability to estimate the bearing of incident acoustic waves. A spatial spectrum of estimated power against bearing can be computed, which can then be processed with a detection threshold to obtain a direction of arrival to any sound sources. This section details the algorithms implemented for this purpose, as well as the array shape estimation

algorithm used to compensate for the movements of the array during data acquisition. The data processing in this work assumes a set of continuous narrow-band signals of known frequencies projected by a target in the far-field of the array (i.e. that the acoustic wave is planar when it impinges upon the array). The direction of arrival estimation algorithms assume spatially and spectrally white noise. This is further discussed in Section III-A.

A. Direction of Arrival Estimation

The bearing to a sound source can be estimated from the acoustic recordings from the hydrophones using various frequency domain narrowband beamforming algorithms, including conventional [30], MVDR [31] and MUSIC [32]. These have been utilized extensively in marine acoustic bearing estimation applications [26], [33], [34], with each of their respective directional power spectra estimated as:

$$P_{\text{conv}}(\theta, f) = \frac{\boldsymbol{a}^{\text{H}}(\theta, f)\hat{\boldsymbol{R}}(f)\ \boldsymbol{a}(\theta, f)}{\boldsymbol{a}^{\text{H}}(\theta, f)\boldsymbol{a}(\theta, f)}, \tag{1}$$

$$P_{\text{mvdr}}(\theta, f) = \frac{1}{\boldsymbol{a}^{\text{H}}(\theta, f)\hat{\boldsymbol{R}}^{-1}(f)\ \boldsymbol{a}(\theta, f)}, \tag{2}$$

$$P_{\text{music}}(\theta, f) = \frac{1}{\boldsymbol{a}^{\text{H}}(\theta, f)\boldsymbol{V}_{\text{n}}(f)\boldsymbol{V}_{\text{n}}^{\text{H}}(f)\boldsymbol{a}(\theta, f)} \tag{3}$$

where θ is the bearing in degrees, f is the frequency, $\boldsymbol{a}$ is the steering vector, $\hat{\boldsymbol{R}}$ is an estimate of the covariance matrix and $\boldsymbol{V}_{\text{n}}$ are the noise subspace eigenvectors of the covariance matrix estimate. The conjugate transpose is denoted as $(\cdot)^{\text{H}}$.

The horizontal plane steering vector [35], $\boldsymbol{a}$, is formulated for arbitrary array geometries with sensor positions at the Cartesian coordinates (x_k, y_k, z_k) for the k^{th} sensor, as depicted in Fig. 2. This follows a left-handed Cartesian reference frame with z as depth, aligning positive rotation about the z axis with navigational bearing, θ, measured clockwise from global North. The steering vector can then be defined as

$$\begin{aligned}\boldsymbol{a}(\theta, f) = \big[1, \quad & \exp(-j2\pi f\delta_2(\theta)/c), \\ & \ldots, \quad \exp(-j2\pi f\delta_K(\theta)/c)\big]^T\end{aligned} \tag{4}$$

where c is the speed of sound, the inter-hydrophone distance in the line of the bearing, $\delta_k(\theta) = x_k \sin\theta + y_k \cos\theta$, and K is the number of sensors.

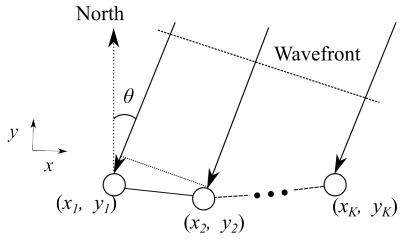

Fig. 2. Array geometry and reference frames for beamformer with an incident wavefront.

The covariance matrix [35] is approximated as a moving average of the cross-spectral matrix, with each time step computed as

$$\hat{\boldsymbol{R}}(f) = \frac{1}{N}\sum_{n=1}^{N} \boldsymbol{U}(n,f)\boldsymbol{U}^{H}(n,f) \tag{5}$$

where N is the number of snapshots used for each time step's estimate, $\boldsymbol{U}(n,f)$ is the array of short time Fourier transformed (STFT) data for all of the sensors. This produces a $K \times K$ cross spectral matrix for each frequency, f, for each time step. For continuous estimation, an exponential moving average can be used,

$$\hat{\boldsymbol{R}}(f,n) = \alpha \boldsymbol{U}(n,f)\boldsymbol{U}^{H}(n,f) + (1-\alpha)\hat{\boldsymbol{R}}(f,n-1) \tag{6}$$

where α is the exponential weighting coefficient.

Each of the direction of arrival estimation methods differ in computational complexity and performance, with a theoretical increased bearing resolution and signal-to-noise ratio increase for MUSIC and MVDR over conventional [19]. In the case of MUSIC this also requires an extra assumption of the number of signal sources present in the data to define the size of the noise subspace.

Accurate knowledge of the sensor positions is required to form the steering vector in order to access the full potential of the more sophisticated algorithms, with incorrect sensor positions causing errors that can lead to misdetections and spurious estimates. Therefore in the case of a severely perturbed dynamic array, it is important to estimate its shape. The commonly used criterion is that an error of $\lambda/10$ in the sensor positions will result in a loss of $1\,\mathrm{dB}$ in conventional beamformer output [20]. For example, at a frequency of $1000\,\mathrm{Hz}$ this would be a deviation of approximately $15\,\mathrm{cm}$ from the assumed positions.

Bearing estimation with beamforming using a linear array results in unresolvable symmetrical detections with respect to the axis of the array, but the magnitude of the false detection can be

reduced through compensating for the array shape [36]. This is a further advantage of correctly estimating the shape of a distorted array, as this left-right ambiguity can potentially be resolved by the array effectively becoming two dimensional [37].

B. Detection and Clustering

An SNR threshold is applied to the beamformer outputs to extract detections of present sound sources. The normalization step is computed as the ratio of the peak to the median value across bearing over a single time sample. Then applying a threshold to this results in a set of detections, each with a pair of associated values: the bearing, θ and the SNR, γ. This produces a set of pairs for the Q peaks at each frequency of interest, f, for each interval of time, t:

$$\Theta_{f,t} = \left\{ \begin{array}{cccc} \theta_{f,t,1}, & \theta_{f,t,2}, & \cdots, & \theta_{f,t,Q} \\ \gamma_{f,t,1}, & \gamma_{f,t,2}, & \cdots, & \gamma_{f,t,Q} \end{array} \right\}. \tag{7}$$

These sets are combined for all frequencies of interest and the mean-shift clustering algorithm [38] is used to associate the peaks from multiple frequencies with a single contact. The result is an estimated number of contacts, $\hat{Q}$, each with an associated bearing and SNR:

$$\hat{\Theta}_t = \left\{ \begin{array}{cccc} \hat{\theta}_{t,1}, & \hat{\theta}_{t,2}, & \cdots, & \hat{\theta}_{t,\hat{Q}} \\ \hat{\gamma}_{t,1}, & \hat{\gamma}_{t,2}, & \cdots, & \hat{\gamma}_{t,\hat{Q}} \end{array} \right\}. \tag{8}$$

C. Array Shape Estimation

The array shape is generally unknown but it can be estimated using the data from non-acoustic sensor modules distributed throughout the array, which provide depth and attitude information. The array can be parameterized as a function of the arbitrary independent variable, r, with the general 3D cubic spline model of the form

$$[x(r), y(r), z(r)] = \left[1, r, r^2, r^3\right] \begin{bmatrix} b_{1,x} & b_{1,y} & b_{1,z} \\ b_{2,x} & b_{2,y} & b_{2,z} \\ b_{3,x} & b_{3,y} & b_{3,z} \\ b_{4,x} & b_{4,y} & b_{4,z} \end{bmatrix} \tag{9}$$

where $[x, y, z]$ are the Cartesian co-ordinates of the array estimate in the same reference frame as Fig. 2. The hydrophone array can then be described as a continuous shape between $r = 0$ and $r = 1$, resulting in a curve that can be defined by the 12 parameters in the matrix of b coefficients, denoted in the following as $\boldsymbol{b}$.

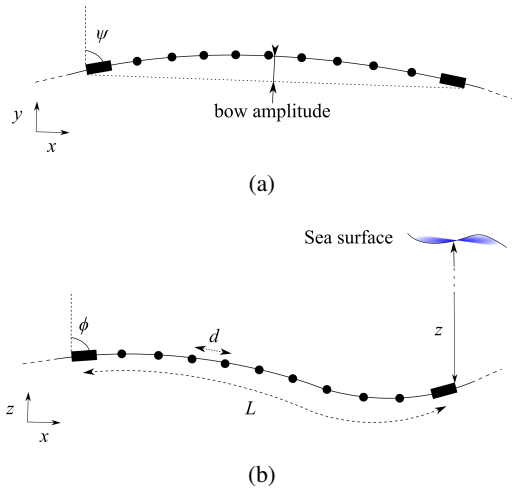

Fig. 3. Array in (a) the horizontal plane (x, y) and (b) the vertical plane (x, z). Dots indicate hydrophones, rectangles indicate non-acoustic sensor modules. Important parameters are labeled: attitude, (ψ, ϕ); inter-hydrophone distance, d; array length, L; and depth, z.

The array used in this work (detailed fully in Section IV-B) had non-acoustic sensor modules at both the head at $r = 0$, and tail at $r = 1$. These provided six measurement inputs to the system: two 2D attitude measurements, denoted by $\boldsymbol{v}(0)$ and $\boldsymbol{v}(1)$; and two depth measurements, denoted by $z(0)$ and $z(1)$ respectively. This renders its state partially observable and unconstrained. In order to reduce the 12 dimensional parameter space of Equation 9, a local coordinate system was defined with its origin at the head of the array. This effectively fixes the three b_1 terms to zero but also excludes the measurement $z(0)$ and reduces the number of measurements by one (9 parameter dimensions, 5 measurement dimensions). Three assumptions are made to further constrain the solution: the length of the array L is fixed; there are no bending moments at the ends of the array, meaning that the curvatures $\kappa(0)$ and $\kappa(1)$ are zero; the overall array curvature $\tilde{\kappa}$ is minimized. These assumptions introduce four regularization constraints to meet the number of parameter dimensions. The spline of best fit is then determined using a non-linear least-squares solver to find the parameters that satisfy the measurements and constraints,

$$\begin{aligned}\hat{\boldsymbol{b}} = \arg\min_{\boldsymbol{b}} \{&\Delta L, \Delta \boldsymbol{v}(0), \Delta \boldsymbol{v}(1), \\ &\Delta z(1), \kappa(0), \kappa(1), A\tilde{\kappa}\}\end{aligned} \tag{10}$$

where $\Delta(\cdot)$ denotes an error term, and A is the curvature weight.

Modeling this array configuration and constraining it in this way results in a couple of implicit limits in the shapes of array that can be estimated (illustrated in Fig. 3): an arc or bow in the

horizontal plane where the shape is only constrained by two direction vectors; and an "S" in the vertical plane where it is constrained by two direction vectors and two depth measurements. For beamforming in the horizontal plane the most salient deformation occurs in the (x, y) plane so the metric of bow amplitude is used to describe the level of deformation the array experiences. This is defined as the largest distance between a point on the array and the line that joins the two endpoints of the array, illustrated in Fig. 3a.

The limitation on the array shape that can be estimated may not be able to accurately model the true shape but will still result in an improved performance if closer than the assumption of a straight array. A further source of error would be from the non-acoustic sensors used to estimate the shape. The higher frequency errors can be smoothed out using a low pass filter with a suitable cutoff frequency, based on the assumption that the errors are Gaussian around the true value.

The constraints and measurement errors were computed in general as follows:

1) Length Error: The length error used to constrain the array estimate to the appropriate length is computed as the difference between the known length of the array and the arc length of the spline,

$$\Delta L = L - \hat{L} \tag{11}$$

where L is the known length of the array ($8\,\mathrm{m}$ in the current study) and the length of the array estimate, $\hat{L}$, is computed as the integral of the Euclidean norm of the first derivative of the spline function,

$$\hat{L} = \int_0^1 |[x'(r), y'(r), z'(r)]|\, dr \tag{12}$$

where $(\cdot)'$ denotes the first derivative with respect to r.

2) Directional Sensor Error: The directional sensor error is the difference between the measured direction vector for that point in the array and that of the spline estimate,

$$\Delta \boldsymbol{v}(r) = \boldsymbol{v}(r) - \hat{\boldsymbol{v}}(r) \tag{13}$$

where $\hat{\boldsymbol{v}}(r)$ is the vector from the model and $\boldsymbol{v}(r)$ is the vector that describes the orientation of the array at the position r along the array. This is derived from the sensor heading, ψ, and pitch, ϕ:

$$\boldsymbol{v}(r) = \boldsymbol{R}_z(r)\boldsymbol{R}_y(r)\boldsymbol{x} \tag{14}$$

where

$$\boldsymbol{R}_z(r) = \begin{bmatrix} \cos(\psi(r)) & -\sin(\psi(r)) & 0 \\ \sin(\psi(r)) & \cos(\psi(r)) & 0 \\ 0 & 0 & 1 \end{bmatrix} \tag{15}$$

$$\boldsymbol{R}_y(r) = \begin{bmatrix} \cos(\phi(r)) & 0 & \sin(\phi(r)) \\ 0 & 1 & 0 \\ -\sin(\phi(r)) & 0 & \cos(\phi(r)) \end{bmatrix} \tag{16}$$

$$\boldsymbol{x} = \begin{bmatrix} 1 \\ 0 \\ 0 \end{bmatrix} \tag{17}$$

The corresponding vector for the array estimate, $\hat{\boldsymbol{v}}(r)$, is computed as the unit vector of the first derivative of the spline function evaluated at the head ($r = 0$) and tail ($r = 1$) ends respectively:

$$\hat{\boldsymbol{v}}_r = \begin{bmatrix} x'(r) \\ y'(r) \\ z'(r) \end{bmatrix} \Bigg/ \left| \begin{bmatrix} x'(r) \\ y'(r) \\ z'(r) \end{bmatrix} \right| \tag{18}$$

3) Depth Sensor Error: The depth sensor error is the difference between the measured depth value at that point in the array (relative to the origin point) and that of the array shape estimate

$$\Delta z(r) = z(r) - \hat{z}(r) \tag{19}$$

where $z(r)$ is the depth sensor estimate (computed from the pressure sensor) and $\hat{z}(r)$ is the z coordinate of the spline function evaluated at the position, r.

4) Minimized Curvature: The spline of best fit is determined by minimizing the curvature of the array estimate, κ, in order to find the least energy spline solution (assuming an array that tends to a straight shape). This is approximated for each position along the array as the magnitude of the second derivative of the spline function,

$$\kappa(r) = \left| [x''(r), y''(r), z''(r)] \right|. \tag{20}$$

To compute the entire array curvature, $\tilde{\kappa}$, the integral is taken across the length of the array

$$\tilde{\kappa} = \int_0^1 \kappa(r) dr. \tag{21}$$

This variable has a weight, A, in the minimization function, chosen to be 0.1 to ensure that the other constraints are prioritized. The measurement-derived constraints are assumed to be of

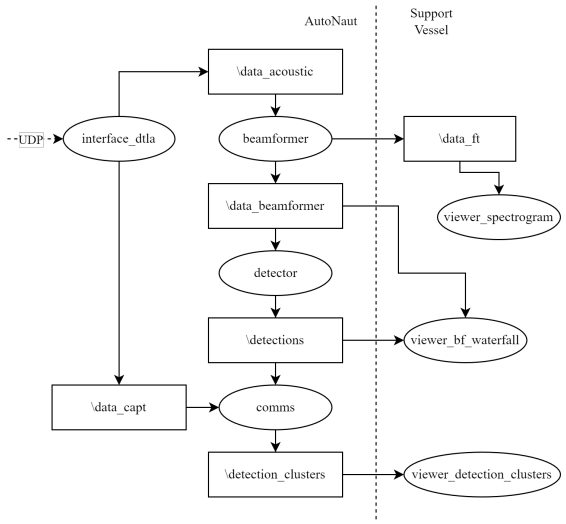

Fig. 4. Software architecture for the onboard real-time processing system, adapted and simplified from the ROS node graph.

the same order of uncertainty and therefore similarly weighted. However, the minimal curvature constraint is an assumed prior and so was chosen to have an order of magnitude less influence on the minimization in order to not over-constrain the solution.

The curvatures at the end positions of the array, $\kappa(0)$ and $\kappa(1)$ for the head and tail end, respectively, are minimized according to the assumption that the array experiences no bending moment around the ends of the array.

D. Hydrophone Position Estimation

The resulting spline function estimated in Section II-C is then used to compute the corresponding Cartesian coordinate estimates of the hydrophones by evaluating the spline function at the along-array locations of the hydrophones, d. These can then be used with (4) to compute the steering vector for the beamforming algorithms described in Section II-A. The array shape estimate will be referred herein as the compensated or corrected result, with the uncompensated result being that of a straight array oriented to the average of the directional sensor data.

III. Real-time Software

The focus of this work was on real-time beamforming and detection. In this context we consider real-time to mean that this processing takes place within the timeframe of the communication system which had an update rate of 16s. Furthermore, it needed to be rapid enough such

that it did not overburden the processor and lead to an accumulating lag. This is distinct from post-processing of the data onshore after the trial as it allows events of interest to be detected and acted upon during operation, within the timeframe of the event occurring. Details on the hardware architecture on which the real-time software was running is provided in Section IV-C.

The Robot Operating System (ROS) [39] was used to implement the real-time processing. It enabled message passing between processing nodes and a modular software layout. It also provided easy tuning and debugging of processing parameters through an ability to playback recorded or simulated data. The developed real-time detection software was written in Python 3.8.10 [40] and the layout of the nodes is as in Fig. 4 with the flow of the processing illustrated in Fig. 5. The signal processing chain includes: an interface node to receive data from the array; this data is then processed with an STFT in order to compute the beamformer result; an SNR threshold is then applied to the beamformer result to extract detections; and finally, the detections are clustered across a time window for all frequencies to estimate the bearing and SNR of each sound source, communicating this to a remote machine. The in-depth function of each node is as follows:

- The *interface_dtla* node handles the raw binary data received from the array, decoding it into segments of acoustic data and non-acoustic sensor data. The acoustic data is broadcast on the ROS topic *data_acoustic* in $0.1\,\mathrm{s}$ snapshots at a rate of $10\,\mathrm{Hz}$ (adjustable based on the required bin width for the STFT. $0.1\,\mathrm{s}$ enables a bin width of $10\,\mathrm{Hz}$) and the non-acoustic sensor data is broadcast on the ROS topic *data_capt* at a rate of $50\,\mathrm{Hz}$. This is illustrated in step (a) of Fig. 5.
- The *beamformer* node computes the Fourier transform of the acoustic data, applies one of the beamforming algorithms detailed in Section II-A and broadcasts the frames of estimated power vs bearing for each frequency of interest on the ROS topic *data_beamformer*. This uses the covariance matrix computed for selected frequencies of interest using an exponential moving average and can be configured to use the desired beamforming algorithm. These steps are illustrated in (b) and (c) of Fig. 5.
- The *detector* node extracts the pertinent information using a $6\,\mathrm{dB}$ threshold on the SNR (found empirically to perform well, although this will depend on the specific environment) in order to determine the presence of a detection as described in Section II-B, outputting the bearing, SNR and frequency. The detections are published on the *detections* ROS topic each time a detection is registered. This is shown in step (d) of Fig. 5.

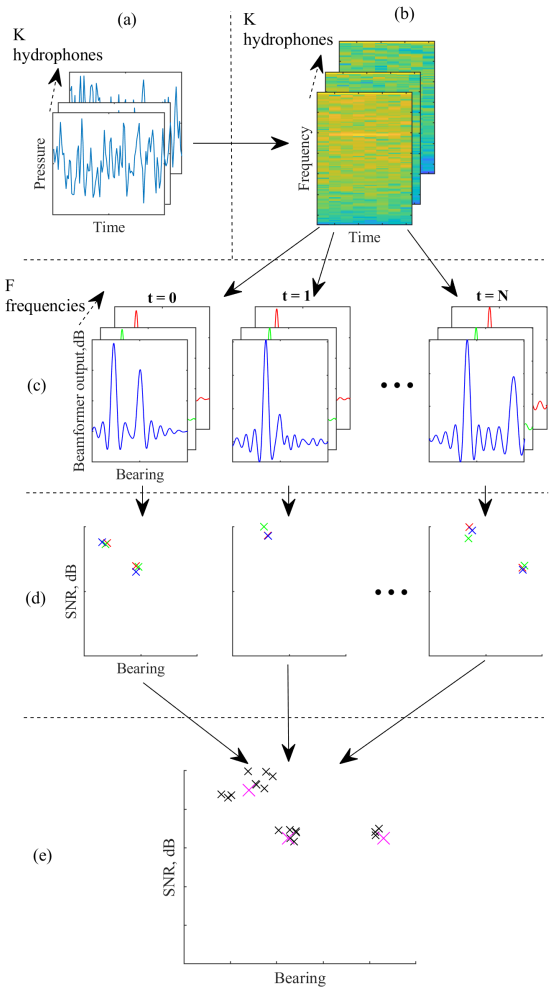

Fig. 5. Illustration of the processing sequence for the real-time system: (a) acoustic data segment from each hydrophone; (b) short-time Fourier transformed data for each hydrophone; (c) beamformed data for each timestep of data segment for each frequency of interest; (d) detections above threshold for each timestep of data segment; (e) detection clusters for the whole segment of data with cluster centers in magenta.

- Finally the *comms* node takes the detection data across a configurable time period and applies the mean-shift clustering algorithm to determine the number of spatially distinct detections and their bearings, with the centers shown in pink. This information can then be broadcast to external systems. This is illustrated in step (e) of Fig. 5.

A. Discussion of Operational Practicalities

As this is a controlled experiment, the frequency content of the signals of interest was known a priori and this allowed selection of a small number of relevant frequency bins. In an operational

scenario, this information would not be known with such precision. In that case, more of the frequency spectrum would need to be investigated and a reasonable number of frequency bins would need to be considered around the expected frequencies. Inclusion of more of the frequency spectrum would require tuning of the detection method to account for the increase in false alarm rate. This could also become computationally expensive and careful consideration would need to be made to ensure that it could be achieved within the computation and energy budget of the vehicle.

For the specific hardware used in this project, detailed fully in Section IV-C, it was within the computational capability of the CPU to process up to approximately 100 frequency bins before a computational bottleneck would occur. If covering more of the spectrum, there are a few strategies for increasing the efficiency of the processing. Increasing the frequency bin width in the STFT step would reduce the number of bins needed to span a given range of the spectrum at the expense of a reduction in the SNR of the output. One could also utilize the Goertzel algorithm [41] to compute the individual frequency bins of interest instead of the entire frequency spectrum. Another potential solution would be to spread the load of the beamforming process over multiple CPU threads, which would allow a large increase in the processing capability at the expense of higher power requirements and heat produced.

IV. Experimental Trial

The experimental trial took place in July 2021 off the coast of Plymouth, UK, at a site where the average depth was around $44\,\mathrm{m}$. The weather for the duration of the two hour trial was sunny and clear, with temperatures around $26\,^{\circ}\mathrm{C}$ and a 8–$10\,\mathrm{kn}$ easterly wind. The sea state was 1-2 with a significant wave height of $<0.5\,\mathrm{m}$. The sound speed profile on the day was decreasing with depth, as shown in Fig. 6, resulting in a downward refracting propagation path and no surface channel.

The mission involved the support vessel towing a sound source emulating an underwater target in the vicinity of an AutoNaut USV deploying a Seiche digital thin line array (DTLA) [42], varying in range between 20–$460\,\mathrm{m}$. The data from the DTLA was recorded and processed in real-time using the software from Section III on bespoke hardware.

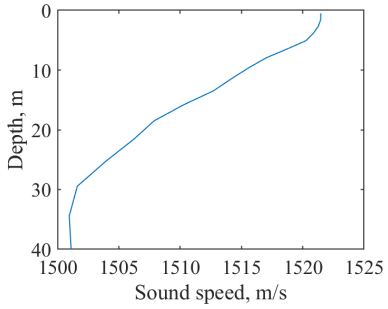

Fig. 6. Sound speed profile for the trial days.

A. AutoNaut USV

The AutoNaut [16] used is a $5\,\mathrm{m}$ long vessel, pictured in Fig. 1, capable of speeds of 1–$3\,\mathrm{kn}$ independent of wave direction. A combination of internal batteries and top-mounted photovoltaic cells were used to power the sensor payload and the auxiliary thruster, which can be used to supplement the wave-propulsion or for control in confined spaces such as deployment from a port or harbor. The AutoNaut was operated from the support vessel via Iridium satellite communications, and instructed to follow a set route autonomously for the duration of the mission.

B. Seiche Digital Thin Line Array

The digital thin line array [42] was developed by Seiche Ltd. as a miniaturized underwater acoustic measurement device designed to be towed from small, low-speed vessels. This was attached at the stern of the AutoNaut and is shown being deployed in Fig. 1. It is $22\,\mathrm{mm}$ in diameter and $20\,\mathrm{m}$ in length, making it sufficiently lightweight and thin to be towed without a significant impact on the speed of the vessel. The 8 high-sensitivity hydrophone sensors are spaced $1\,\mathrm{m}$ apart and sampled at $48\,\mathrm{kHz}$ with co-located $20\,\mathrm{bit}$ ADCs to digitize the signal prior to transmission to the interface board, providing a high signal-to-noise ratio. As well as hydrophones the array is also equipped with 3-axis compass, attitude, pressure and temperature (CAPT) modules, one at either end of the acoustic section, $50\,\mathrm{cm}$ outside each of the end hydrophones. These allow the orientation of the array to be compensated for when computing bearing estimates, and also potentially to estimate the shape of the array when perturbed, as described in Section II-C. The array deployment depth was found to vary between 4 and $11\,\mathrm{m}$.

C. Onboard Real-time Processing

The onboard real-time processing hardware is contained in a peli-case stored in the water-tight compartment of the AutoNaut, shown in Fig. 7a. The internal connections and physical configuration are as shown in Fig. 7c and 7b, respectively.

The main computing device (green) is a LattePanda Delta 432 with $4\,\mathrm{GB}$ of RAM and an Intel Celeron N4100 processor running Ubuntu 20.04. This receives the data from the DTLA top-interface boards (dark blue) via Ethernet and transmits detection information to an external PC also via Ethernet. Connected over USB are the SSD (yellow), on which all the data are stored for post-processing, and the GPS unit (orange), used to synchronize the computer's clock to UTC and provide accurate timestamps for data. Both the top-interface board and the main computing device are powered by the onboard AutoNaut power systems, running through an uninterruptible power supply (UPS) (cyan) for robustness against power dropouts and with a manual hardware switch for power-cycling. All external connections are waterproof through a sealed external plate (magenta).

D. Sound Source

The sound source used to mimic an underwater target was a $16\,\mathrm{cm}$ diameter ITC-1007 ball projector deployed from the $12\,\mathrm{m}$ support vessel at an approximate depth of $5\,\mathrm{m}$. This was constantly projecting tonal signals at the frequencies detailed in Table I, with the frequencies used for detection chosen to be at approximately the $\lambda/2$ design frequency of the array (up to $\sim 750\,\mathrm{Hz}$) in order to avoid spatial undersampling.

The source levels were estimated using the array in a controlled harborside test. This was carried out at a range of approximately one metre using a single hydrophone on the DTLA and the source suspended in the water. The source level was then estimated using the receive level on the hydrophone.

V. Results

A. Array Motion

Both the AutoNaut and the source-carrying support vessel were logging their GPS coordinates, the tracks of which are shown in Fig. 8f. These are shown in relative Cartesian coordinates computed from the UTM coordinates of the GPS data, where the origin of the axis is set to the

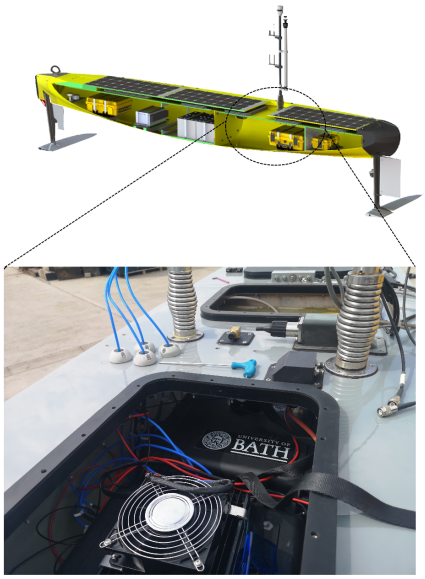

(a)

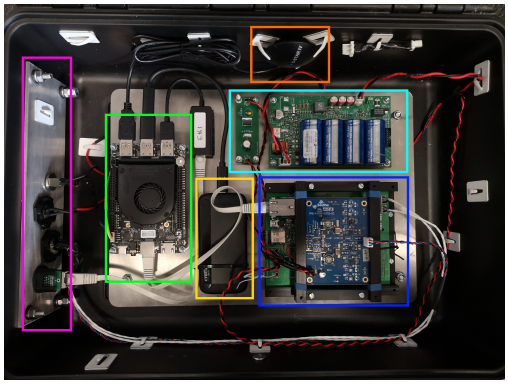

(b)

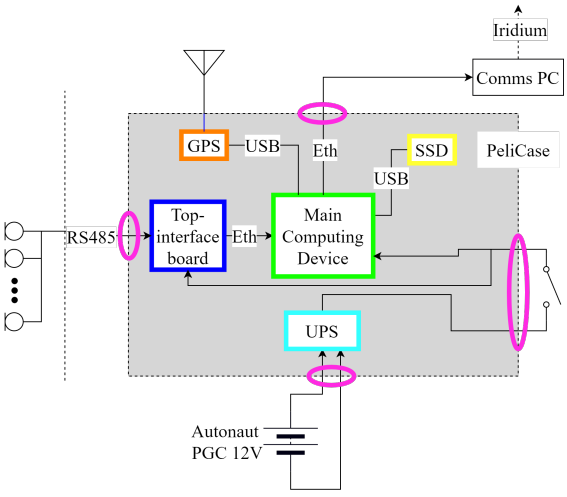

(c)

Fig. 7. Onboard processing system (a) onboard location, (b) physical layout and (c) hardware diagram.

TABLE I

SOURCE LEVELS AT THE FREQUENCIES EMITTED BY THE PROJECTOR (ESTIMATED)

Frequency, Hz	Source level, dB
480	93
650	100
700	104
750	102
800 (unused)	107
1120 (unused)	115
1630 (unused)	126

beginning of the AutoNaut track. The support vessel track aimed to provide a variety of bearings and ranges between the array and the source.

Prior to their inclusion in the shape estimation process, the depth and heading/pitch measurements were filtered with a 7^{th} order low pass IIR filter with a cutoff of $0.2\,\text{Hz}$. These values were selected as these bands contain 99% of the power in the data. The filtered data for the head and the tail sensors are shown in Fig. 8(b-d). The status of the auxiliary thruster in 8(a). The bow amplitude of the array shape estimate from the spline interpolation in 8(e). Bow amplitude is the magnitude of the perturbation from the line between the positions of each end sensor, illustrated in Fig. 3a.

Consider from the start of the run to 13:45:00 in Fig. 8, when the thruster was running as shown in Fig. 8a. Fig. 8b shows that the heading measured at the head and tail ends of the array and by the AutoNaut itself are similar, suggesting that the array was likely to be approximately straight. However, this is up to roughly $90°$ to the course of the AutoNaut which is due to the North-Westerly tidal stream current [43] causing the AutoNaut to move with a crabbing motion. There are periods of the head and tail heading differing by approximately $45°$, such as at 13:30 and 13:45. These are believed to be caused by an impulse from a particularly large wave whipping the tail out, which then remains relatively static for a period until further propulsion brings the array back to straight. Apart from these brief exceptions the estimated bow amplitude of the array is generally less than $0.5\,\text{m}$ for this first section of data, shown in Fig. 8e.

The tidal current speed reduces and becomes almost slack at 14:10:00 before changing to an Easterly direction, during which the thruster is turned off, and the array and AutoNaut heading more closely matches the AutoNaut course. However, there is a larger disparity between the

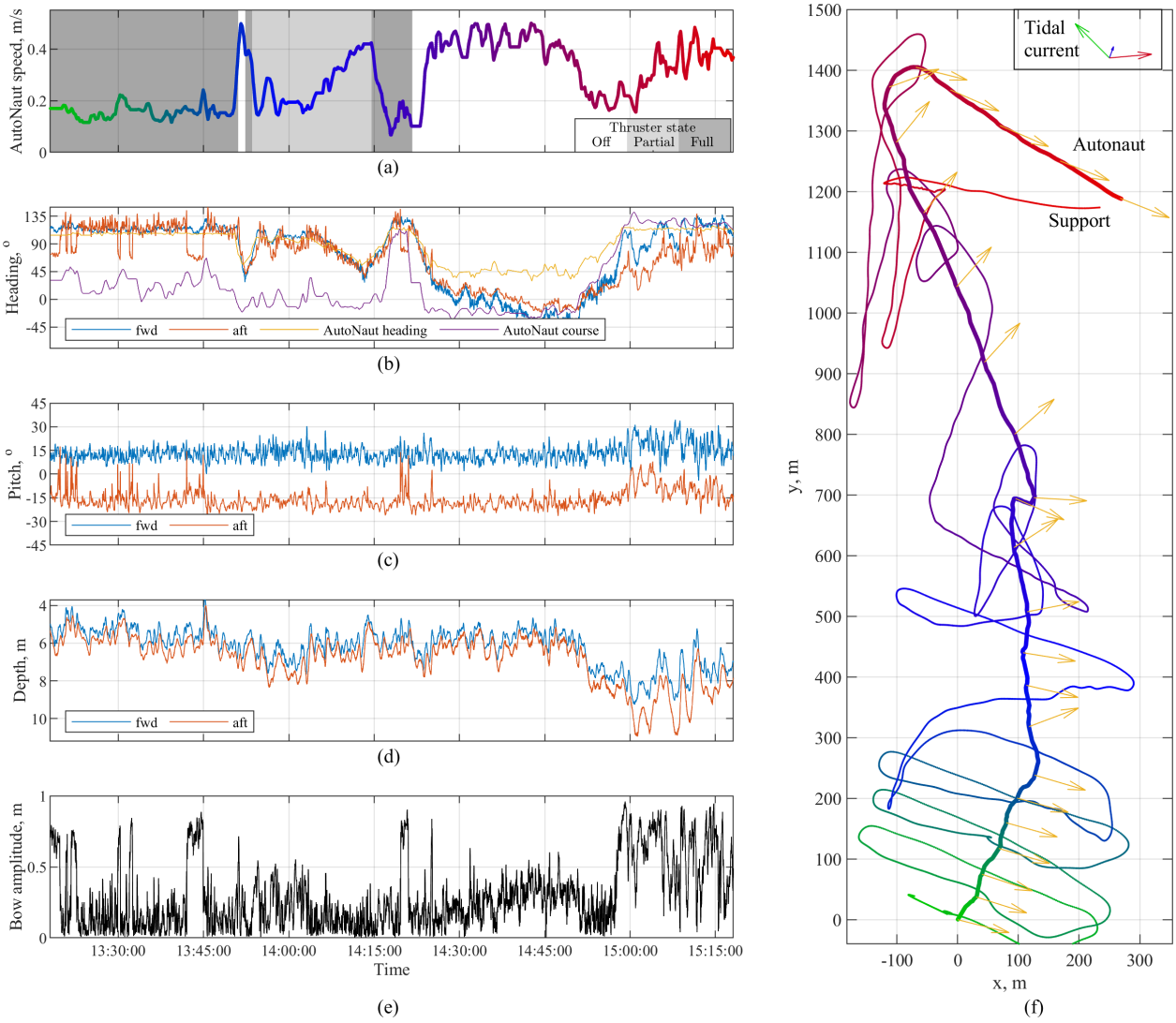

Fig. 8. Non-acoustic filtered experimental data: (a) the AutoNaut speed derived from the GPS track (color corresponds to the time from the GPS track in (f)) and the auxiliary thruster status ; (b) filtered data from array heading sensors, AutoNaut heading and the direction of the AutoNaut's motion; (c) filtered data from array pitch sensors; (d) filtered data from depth sensors; (e) bow amplitude of estimated array shape from spline fit; and (f) GPS track for support vessel (thin) and AutoNaut (thick), with the color corresponding to (a). AutoNaut heading is shown at regular intervals with yellow arrows and the direction of the tidal current is shown in the top left arrows, with color corresponding to the GPS tracks.

array head and tail heading estimates, resulting in a larger estimated bow amplitude. This occurs because the array is not being pulled as taut as when the current strongly opposes the direction of motion, hence also the array depth increasing.

Throughout the dataset the pitch measurements of both the head and tail of the array remain consistently the inverse of one another. This suggests the array is sagging in the middle with

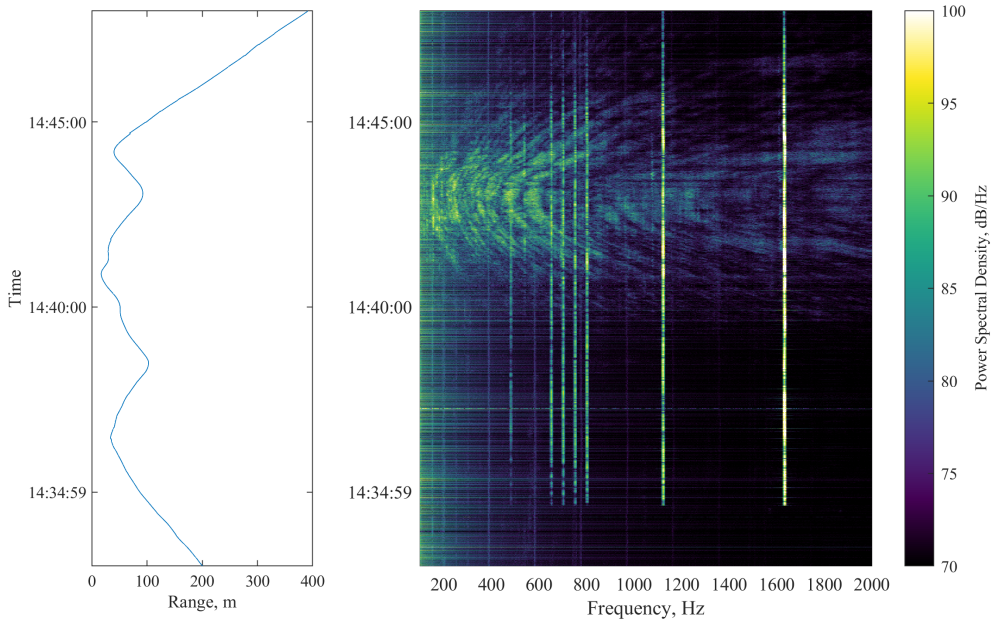

(a) (b)

Fig. 9. (a) Range to support vessel computed using GPS coordinates and (b) spectrogram of acoustic data from a single hydrophone. The sound source was turned on at the beginning of the run at 14:34 and was switched off at the end of the run at 15:06.

both ends pointing slightly up, probably the result of the ballast distribution. Each depth sensor's data is also roughly similar, suggesting that the array is mostly horizontal in the water. However, after 15:00 the disparity between the depth sensors increases suggesting that array is tilting along its axis. Also notably the tail-end sensor experiences a lot more motion in both heading and pitch than the head-end sensor, due to the whipping motion of the end of the array.

B. Acoustic data

The acoustic data from a single hydrophone can be viewed as a spectrogram, as shown in Fig. 9b with the corresponding range to the support vessel in Fig. 9a computed from the GPS coordinates. The increase and decrease in SNR of the source signal is clearly visible, shown by the linear features of constant frequency at each of the frequencies being projected. At 14:40:00 there is also the characteristic pattern of the Lloyd's mirror effect [44] from the support vessel's engine as it passed the array. There was little evidence of flow noise at the frequencies of interest, although the lower frequencies more likely to be affected [45] were not investigated.

C. Beamforming Algorithms

Combining the data from each hydrophone using each of the three beamforming algorithms introduced in Section II-A results in the bearing plots shown in Fig. 10. The MUSIC output is shown for the assumption of both one and two signals. The ground truth, overlaid in magenta, was computed as the bearing from the AutoNaut to the support vessel from their GPS coordinates, and is therefore less accurate at close ranges because of the offset of the array behind the AutoNaut and the source behind the tow vessel. Despite this, it shows good agreement between the estimate and the ground truth at points of high SNR.

The conventional beamformed result has the highest SNR and the lowest angular resolution. The MUSIC result has the lowest SNR and the highest angular resolution, and the MVDR characteristics fall in between these two. Another feature of note is what appears to be a second distinct arrival after roughly 15:00 when the array becomes slightly tilted, which can be attributed to multipath reflections. This is not captured by conventional beamforming but is with MVDR and MUSIC with the assumption of two signals. MUSIC with the assumption of a single signal only captures the strongest arrival.

D. Array Shape Compensation

The estimated shapes were used to compute the array steering vector and the beamformer outputs were recomputed in order to investigate the effect of compensating for the perturbed array. As the MUSIC algorithm is most sensitive to sensor position errors, it also has the most potential for gain increase after compensation. Fig. 11 shows a comparison of the MUSIC outputs for two frequencies using a section of the data shown in Fig. 9b for which there is estimated to be a substantial perturbation of the array. The array shape compensated result for $480\,\mathrm{Hz}$ shown in Fig. 11b shows a removal of the ambiguity, leaving only the correct detection. However, compensation is shown to remove the true detection for $650\,\mathrm{Hz}$, as shown in Fig. 11d, suggesting that the array shape at this point might be more complex than can be estimated with the available data and that the prior assumption of a bow shape is invalid. Nevertheless, the peak SNR value is found to increase in both cases (although at the latter frequency this is the ambiguous peak).

A comparison between beamformers of the difference in SNR caused by compensation is shown in Fig. 12. This was computed at all source frequencies for every frame in which a signal was estimated to be present, using an SNR threshold of $6\,\mathrm{dB}$ on the uncompensated beamformer

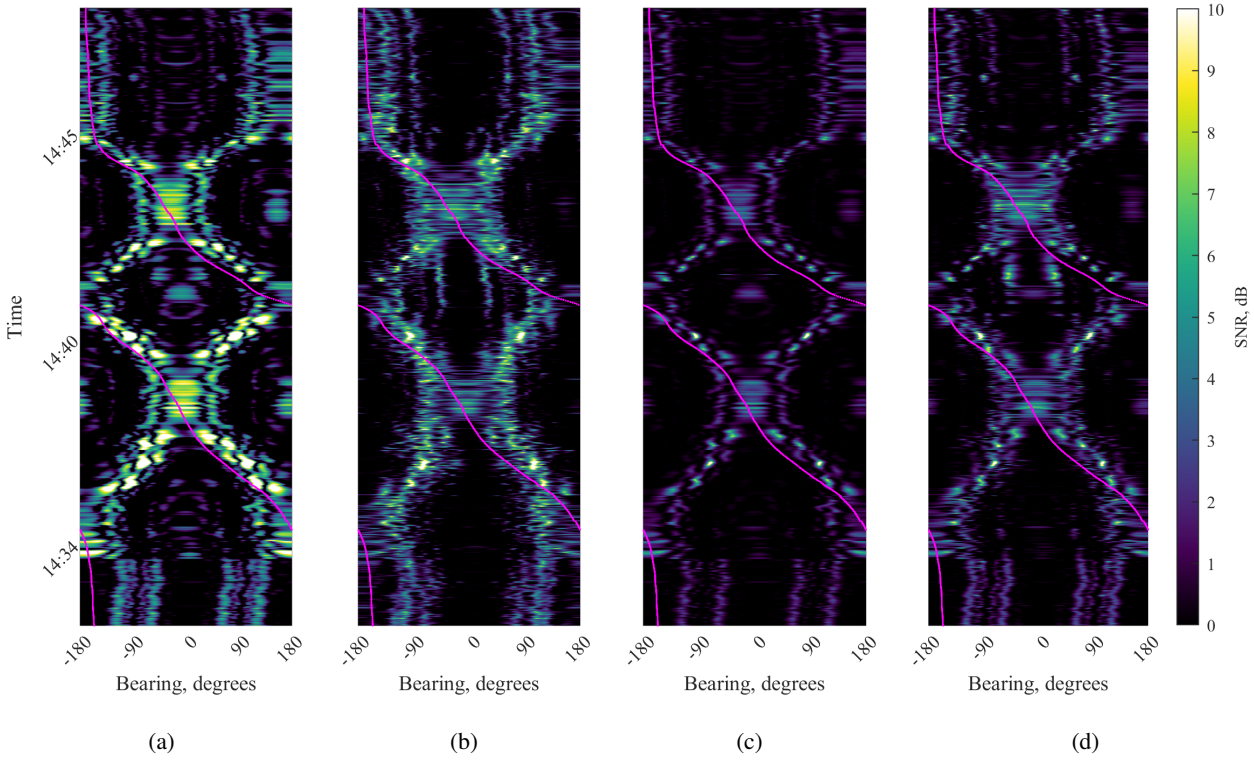

Fig. 10. Comparison of the SNR relative to median for the (a) Conventional beamformer, (b) MVDR, (c) MUSIC with 1 signal, and (d) MUSIC with 2 signals, for the 700 Hz band.

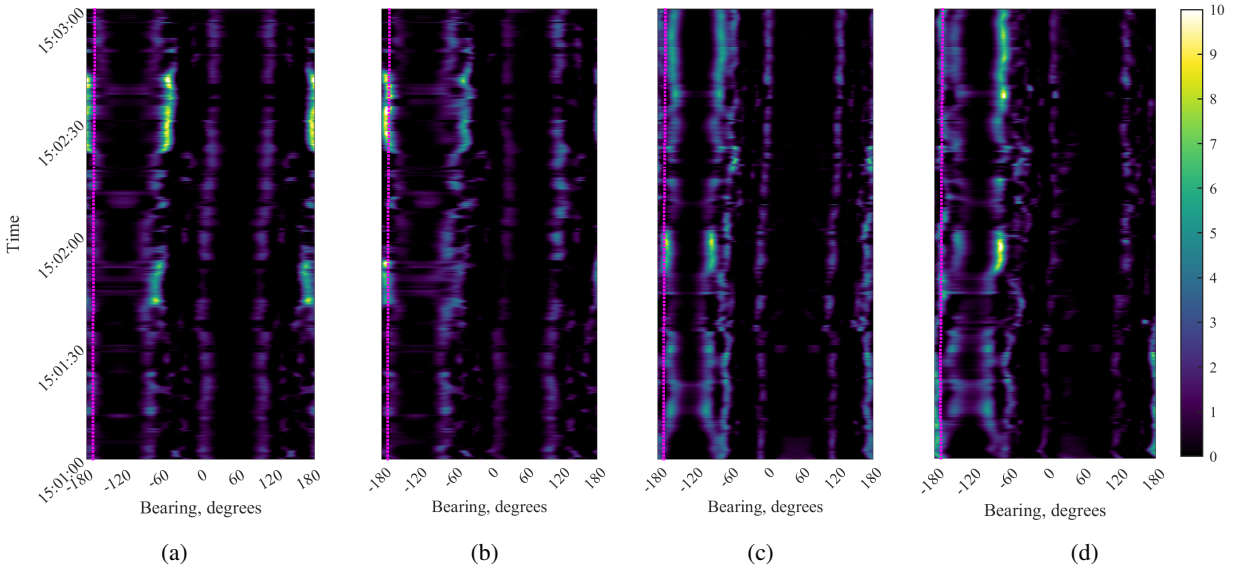

Fig. 11. Comparison of the SNR of the MUSIC algorithm with two signals using the steering vector formulated using the uncompensated straight array for 480 Hz (a) and 650 Hz (c) and compensated spline-fit shape estimates for 480 Hz (b) and 650 Hz (d). The magenta line is the ground truth computed using the GPS coordinates.

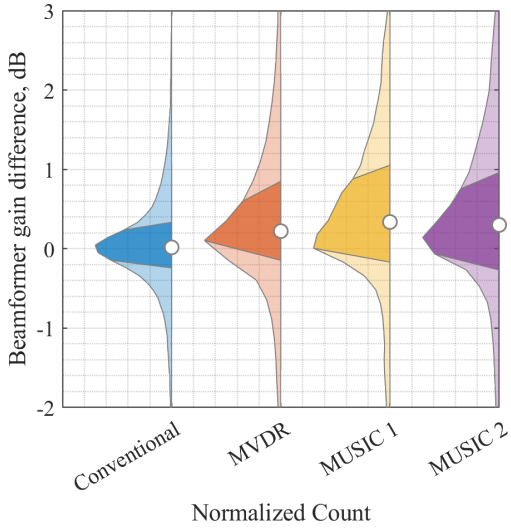

Fig. 12. Half-violin plots of the distribution of snapshot beamformer spectrum maximum output difference for each method as a result of compensation with the spline-fit estimate for snapshots above an SNR threshold of $6\,\mathrm{dB}$, measured at the uncompensated beamformer output. Central point shows the median, with the lighter shaded area illustrating the upper and lower quartiles. Note, the plots extend beyond the bounds of the y axis limits.

output. For conventional beamforming it can be seen to have made a negligible difference. For both MVDR and MUSIC, compensation made a marginal improvement in the SNR on average. For the most improved method, MUSIC, there is an increased beamformer performance 75% of the time when using the compensated result, with a median increase of $0.38\,\mathrm{dB}$ and a maximum increase of $5.8\,\mathrm{dB}$.

Based on this array configuration ($8\,\mathrm{m}$ long with CAPT modules at either end) and the results from this work, there is no benefit to performing array shape estimation because of the marginal improvement it provides to MVDR and MUSIC performance and the added processing complexity. Furthermore, the uncertainty in the accuracy of the ambiguity removal indicates that the array's non-acoustic instrumentation is not sufficient to fully capitalize on the potential angular resolution improvements, as the underlying assumption of a bow shape in the horizontal plane is found to sometimes be invalid. The use of MVDR or MUSIC without shape estimation could still be beneficial for their ability to resolve closely spaced sources, albeit at the cost of SNR.

A limitation of this study is the lack of available ground truth for the position and shape of the array, and also the specific location of the sound source. This means an assessment of the potential optimal performance of the system is not possible. This could be improved by more

densely instrumenting the array or with more accurate knowledge of the source level of the projector. A further limitation is that this study only contains the data from a single trial and therefore is limited to the sea and weather conditions on that date.

E. Real-time Reporting

The real-time system described in Section III was operating during the sea trial described in Section IV. An exponential moving average was used for covariance matrix estimation (described in Section II-A) with a coefficient of 0.9 and a 0.5 snapshot overlap. Detection data across a 16 second time window was used for the clustering, decided as a suitable period of time across which to aggregate detections, taking into account computational and operational considerations.

The system has a number of viewer modules which were used to analyze and observe the results in real-time. Fig. 13 shows the beamformer output with the corresponding detections overlaid. Due to the assumption of a straight array, this is only shown for the single sided spatial spectrum. The alternating cyan and magenta colors show the separate 16 second sections of data used to aggregate each subsequent detection cluster, denoted by the $\times$ symbols. These aggregated detections can also be displayed across a longer period of time to show the movement of the sound source, as another bearing-time plot as in Fig. 14 or on a Cartesian axis with the GPS coordinates, as in Fig. 15. In practice the sound source GPS location would not be known but has been provided in this re-creation to show the correlation between the bearings of the detections and that of the source. These aggregated detections were sent to shore over Iridium every 3 minutes to be visualized on a map in a similar manner to that of Fig. 15.

VI. Summary

This work presents the first demonstration of direction of arrival estimation via beamforming from a towed hydrophone array deployed behind an AutoNaut wave-propelled USV. Three Fourier domain beamforming algorithms were applied to the data, with conventional beamforming found to have the highest SNR, and MUSIC to have higher spatial resolution. Hydrophone positions estimated from a cubic spline fit to the non-acoustic sensor data were used to try and ameliorate the effect of the perturbed array shape. This was found to have negligible effect on conventional beamforming but provided a marginal median increase of $0.38\,\mathrm{dB}$ and a maximum of $5.8\,\mathrm{dB}$ in MUSIC beamformer performance. It was also found to potentially reduce the severity of the left-right ambiguity, although some instances resulted in a degradation

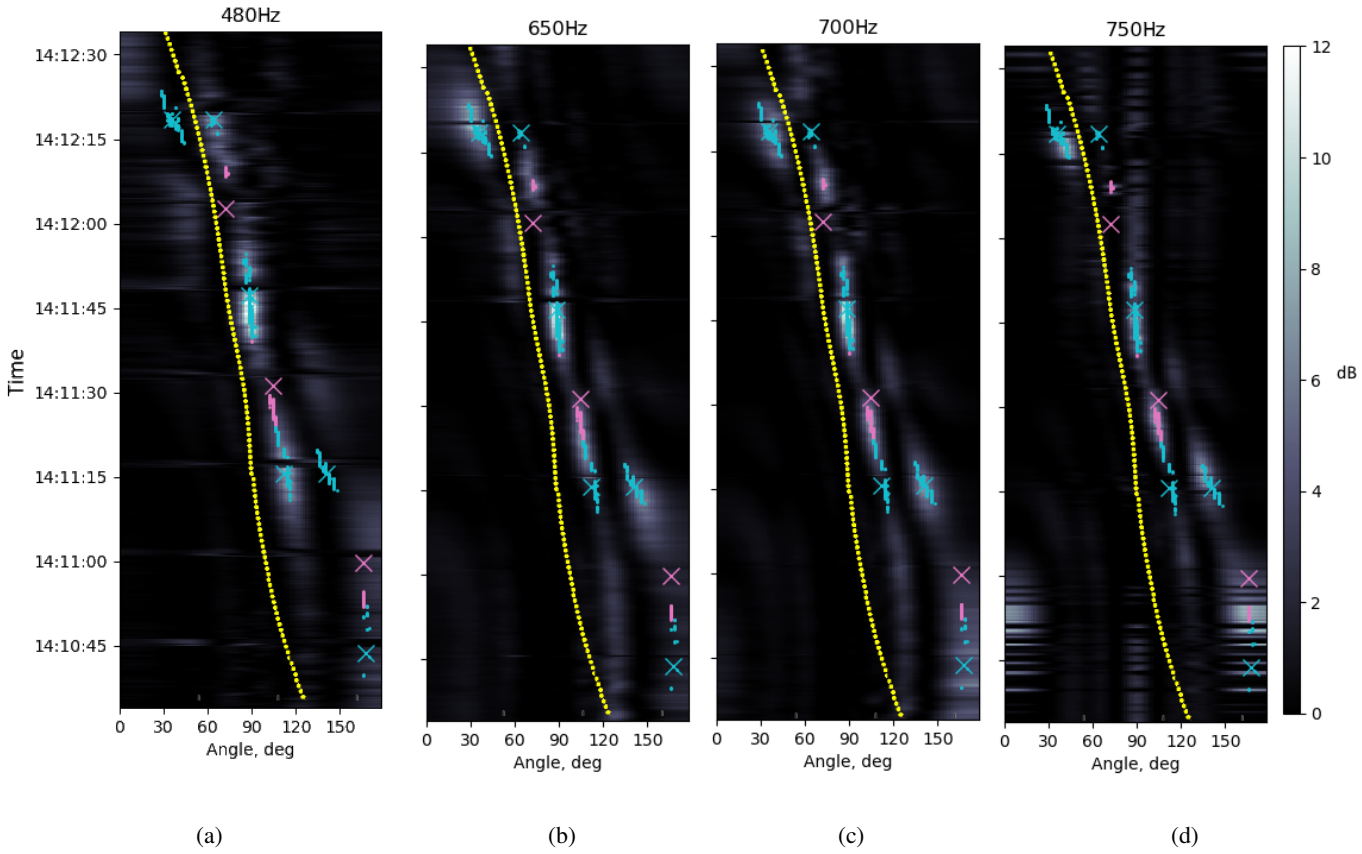

(a) (b) (c) (d)

Fig. 13. MUSIC algorithm output from the real-time system (captured on the support PC) with the corresponding detections (dots) and the aggregated detections (crosses). Alternating magenta and cyan colors indicate alternate 16 s data intervals. Overlaid yellow is the ground truth computed in post from the GPS co-ordinates of AutoNaut and the support vessel.

of performance, indicating that the underlying assumptions in the model are sometimes invalid. In future work, it would be interesting to more densely instrument the array to further investigate the use of the more sophisticated algorithms, but based on the configuration used in this work, conventional beamforming would be recommended for its robustness against sensor position errors. Furthermore it would also be valuable to assess the performance of the passive acoustic system in different sea states and weather conditions.

Finally, this paper presents a real-time in-situ processing system capable of detection and bearing estimation, reporting these results remotely to a shoreside operator. In its current form, this uses the average array sensor heading and the assumption of a straight array to beamform the acoustic data, broadcasting aggregated detections. The outcomes of this work demonstrate that the AutoNaut, with its low carbon footprint and potential for persistent operations, is an

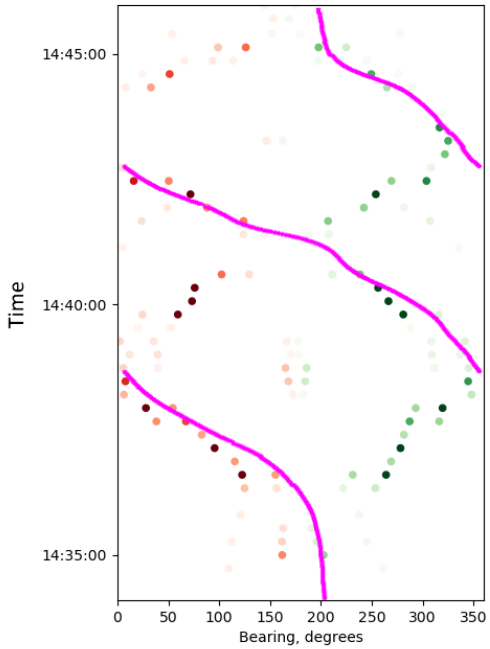

Fig. 14. Detection clusters for 16 second intervals for the experimental dataset from the real-time system. Red/green hue are the ambiguous detections resulting from the linear array assumption and color value indicates the average SNR of the detection cluster. Overlaid magenta is the ground truth computed in post from the GPS co-ordinates of AutoNaut and the support vessel.

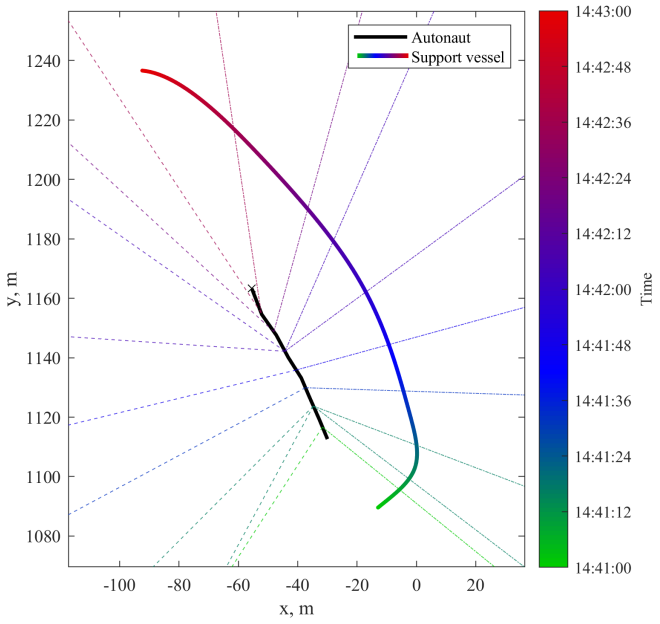

Fig. 15. Re-creation of end output at operator's terminal. Dashed and solid lines indicate detections out of the port and starboard sides of the AutoNaut, respectively.

effective platform for passive acoustic monitoring when towing an acoustic array.

ACKNOWLEDGMENT

This work was funded by the Engineering and Physical Science Research Council (EPSRC) Impact Acceleration Account (grant no. IAA-411) and the European Defence Agency (EDA) Open Cooperation for European Maritime Awareness (OCEAN2020). The authors would like to thank Mark Burnett, Jesse Loynes, Richard Schofield and David Maclean at Seiche Ltd. and AutoNaut for their support during the trial.

REFERENCES

[1] T. Daniel, J. Manley, and N. Trenaman, "The Wave Glider: Enabling a new approach to persistent ocean observation and research," *Ocean Dynamics*, vol. 61, pp. 1509–1520, 2011.

[2] P. Johnston and M. Poole, "Marine surveillance capabilities of the AutoNaut wave-propelled unmanned surface vessel (USV)," in *OCEANS 2017 - Aberdeen*, 2017, pp. 3–6.

[3] D. Webb, P. Simonetti, and C. Jones, "Slocum: an underwater glider propelled by environmental energy," *IEEE Journal of Oceanic Engineering*, vol. 26, no. 4, pp. 447–452, 2001.

[4] C. Eriksen, T. Osse, R. Light, T. Wen, T. Lehman, P. Sabin, J. Ballard, and A. Chiodi, "Seaglider: a long-range autonomous underwater vehicle for oceanographic research," *IEEE Journal of Oceanic Engineering*, vol. 26, no. 4, pp. 424–436, 2001.

[5] J. D. Holmes, W. M. Carey, J. F. Lynch, A. E. Newhall, and A. Kukulya, "An autonomous underwater vehicle towed array for ocean acoustic measurements and inversions," in *Oceans 2005 - Europe*, vol. 2. IEEE, 2005, pp. 1058–1061.

[6] P. Hursky and M. Porter, "Glider towed array tests during the Makai experiment," *Proceedings of the Eigth European Conference on Underwater Acoustics, 8th ECUA*, pp. 1–9, 2006.

[7] J. A. Hildebrand, G. L. D'Spain, and M. A. Roch, "Glider-based Passive Acoustic Monitoring Techniques in the Southern California Region," *Sea Technology*, no. 1, pp. 28–32, 2009.

[8] P. Gemelli, P. M. Poulain, M. I. Zignego, and D. Cecchi, "Slocum underwater glider acoustic capabilities improvement by wings re-design," in *2019 IMEKO TC19 International Workshop on Metrology for the Sea: Learning to Measure Sea Health Parameters, MetroSea 2019*, vol. 1, no. 69, 2020, pp. 179–183.

[9] E. T. Küsel, T. Munoz, M. Siderius, D. K. Mellinger, and S. Heimlich, "Marine mammal tracks from two-hydrophone acoustic recordings made with a glider," *Ocean Science*, vol. 13, no. 2, pp. 273–288, 2017.

[10] A. Tesei, R. Been, D. Williams, B. Cardeira, D. Galletti, D. Cecchi, B. Garau, and A. Maguer, "Passive acoustic surveillance of surface vessels using tridimensional array on an underwater glider," *MTS/IEEE OCEANS 2015 - Genova: Discovering Sustainable Ocean Energy for a New World*, 2015.

[11] C. Tucker, "Anti-submarine warfare (ASW) towed array capability for unmanned and small platforms," *Undersea Defence Technology (UDT) 2019*, 2019.

[12] J. E. Manley and G. Hine, "Unmanned Surface Vessels (USVs) as tow platforms: Wave Glider experience and results," *OCEANS 2016 MTS/IEEE Monterey, OCE 2016*, 2016.

[13] S. Wiggins, J. Manley, E. Brager, and B. Woolhiser, "Monitoring marine mammal acoustics using wave glider," *MTS/IEEE Seattle, OCEANS 2010*, pp. 8–11, 2010.

[14] B. Bingham, N. Kraus, B. Howe, L. Freitag, K. Ball, P. Koski, and E. Gallimore, "Passive and active acoustics using an autonomous wave glider," *Journal of Field Robotics*, vol. 29, no. 6, pp. 911–923, 2012.

[15] V. E. Premus, P. A. Abbot, V. Kmelnitsky, C. J. Gedney, T. A. Abbot, and Heath Hands, "A wave glider-based, towed hydrophone array system for autonomous, real-time, passive acoustic marine mammal monitoring," *The Journal of the Acoustical Society of America*, vol. 152, no. 3, pp. 1814–1828, sep 2022.

[16] P. Johnston, "Passive Acoustic Monitoring By USV: Wave-propelled AutoNaut Comes of Age," *Ocean News Technology EDITORIAL*, 2017.

[17] P. Johnston and C. Pierpoint, "Deployment of a Passive Acoustic Monitoring (PAM) array from the AutoNaut wave-propelled Unmanned Surface Vessel (USV)," *OCEANS 2017 - Aberdeen*, pp. 0–3, jun 2017.

[18] H. L. Van Trees, *Optimum Array Processing: Part IV of Detection, Estimation, and Modulation Theory*, ser. Detection, Estimation, and Modulation Theory. Wiley, 2004.

[19] A. Anthony Treloar, "Passive Acoustic Array Modelling and Processing for a Wave-Propelled Unmanned Surface Vessel," Ph.D. dissertation, University of Bath, 2022.

[20] S. E. Dosso and B. J. Sotirin, "Optimal array element localization," *The Journal of the Acoustical Society of America*, vol. 106, no. 110, pp. 3445–3459, 1999.

[21] D. E. Wahl, "Towed array shape estimation using frequency-wavenumber data," *IEEE Journal of Oceanic Engineering*, vol. 18, no. 4, pp. 582–590, 1993.

[22] H. Bucker, "Beamforming a Towed Line Array of unknown shape," *Journal of Acoustical Society of America*, vol. 63, no. 5, pp. 1451–1454, 1978. [Online]. Available: http://dx.doi.org/10.1121/1.381890http://asa.scitation.org/toc/jas/63/5

[23] N. L. Owsley and G. R. Swope, "Time delay estimation in a sensor array," *Underwater Acoustics and Signal Processing*, vol. 1, no. 1, pp. 421–432, 1981.

[24] A. J. Weiss and B. Friedlander, "Array shape calibration using eigenstructure methods," in *Conference Record - Asilomar Conference on Circuits, Systems & Computers*, vol. 2. Maple Press, Inc, 1989, pp. 925–929.

[25] P. Gerstoft, W. S. Hodgkiss, W. A. Kuperman, H. Song, M. Siderius, and P. L. Nielsen, "Adaptive Beamforming of a Towed Array During a Turn," *IEEE Journal of Oceanic Engineering*, vol. 28, no. 1, pp. 44–54, 2003. [Online]. Available: http://pgerstoft.ucsd.edu/papers/Gerstoft2003Turn.pdf

[26] Z. Zheng, T. C. Yang, P. Gerstoft, and X. Pan, "Joint towed array shape and direction of arrivals estimation using sparse Bayesian learning during maneuvering," *The Journal of the Acoustical Society of America*, vol. 147, no. 3, pp. 1738–1751, 2020.

[27] N. Convers Wyeth, "Methods of array element localization for a towed underwater acoustic array," *IEEE Journal of Oceanic Engineering*, vol. 19, no. 1, pp. 128–133, 1994. [Online]. Available: http://ieeexplore.ieee.org/document/289457/

[28] G. S. Egeland, "Array Shape Estimation," *OCEANS 82*, vol. Sept, no. 6, pp. 121–122, 1982.

[29] J. L. Odom and J. L. Krolik, "Passive Towed Array Shape Estimation Using Heading and Acoustic Data," *IEEE Journal of Oceanic Engineering*, vol. 40, no. 2, pp. 465–474, 2015.

[30] M. S. Bartlett, "Periodogram analysis and continuous spectra," *Biometrika*, vol. 37, no. 1/2, pp. 1–16, jun 1950.

[31] J. Capon, "High-resolution frequency-wavenumber spectrum analysis," *Proceedings of the IEEE*, vol. 57, no. 8, pp. 1408–1418, 1969.

[32] R. Schmidt, "Multiple Emitter Location and Signal Parameter Estimation," *IEEE Transactions on Antennas and Propagation*, vol. 34, no. 3, pp. 276–280, Mar 1986.

[33] L. Fillinger, A. J. Hunter, M. Zampolli, and M. C. Clarijs, "Passive acoustic detection of closed-circuit underwater breathing apparatus in an operational port environment." *The Journal of the Acoustical Society of America*, vol. 132, no. 4, 2012.

[34] Q. Wang, B. Zhou, Y. Chen, and H. Quan, "Subarray Beam-space Adaptive Beamforming Combined with Array Shape Estimation based on Non-Acoustic Sensor," *Acoustical Physics*, vol. 65, no. 2, pp. 226–233, 2019.

[35] H. Krim and M. Viberg, "Two decades of array signal processing research: the parametric approach," *IEEE Signal Processing Magazine*, vol. 13, no. 4, pp. 67–94, 1996.

[36] K. Kaouri, "Left-Right Ambiguity Resolution of a Towed Array Sonar," Ph.D. dissertation, 2000.

[37] S. M. Jesus, P. Felisberto, and F. Coelho, "Towed array geometry estimation during ship's maneuvering," *The Journal of the Acoustical Society of America*, vol. 96, no. 5, pp. 3312–3312, 1994.

[38] D. Comaniciu and P. Meer, "Mean shift: A robust approach toward feature space analysis," *IEEE Transactions on Pattern Analysis and Machine Intelligence*, vol. 24, no. 5, pp. 603–619, 2002.

[39] M. Quigley, B. Gerkey, K. Conley, J. Faust, T. Foote, J. Leibs, E. Berger, R. Wheeler, and A. Ng, "ROS: an open-source Robot Operating System," Tech. Rep.

[40] G. Van Rossum and F. L. Drake, *Python 3 Reference Manual*. Scotts Valley, CA: CreateSpace, 2009.

[41] G. Goertzel, "An algorithm for the evaluation of finite trigonometric series," *The American Mathematical Monthly*, vol. 65, no. 1, pp. 34–35, 1958.

[42] "Seiche Digital Thin Line Array Product Datasheet," https://www.seiche.com/showcase/single-pam-hydrophone/.

[43] "Tidal Streams, West Country, Falmouth to Teignmouth," 2022. [Online]. Available: https://www.visitmyharbour.com/articles/3178/tidal-streams-west-country-falmouth-to-teignmouth

[44] W. M. Carey, "Lloyd's Mirror—Image Interference Effects," *Acoustics Today*, vol. 5, no. 2, pp. 14–20, 2009.

[45] K. Karthik, S. Jeyakumar, and J. S. Sebastin, "Numerical prediction of flow noise levels on towed sonar array," *Proceedings of the Institution of Mechanical Engineers Part M: Journal of Engineering for the Maritime Environment*, vol. 235, no. 2, pp. 600–606, 2021.

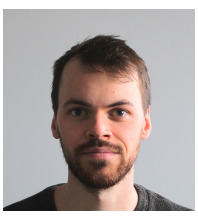

Alfie Anthony Treloar Alfie Anthony Treloar received the M.Eng degree in mechanical engineering with industrial placement and the Ph.D degree in the field of passive sonar modeling and processing from the University of Bath, Bath, U.K. in 2016 and 2022 respectively. In 2015 and 2016 he worked as a research assistant in robotics and sonar as well as being involved in a start-up company incubated at the University. Since 2021 he has worked as a Research Associate with the University of Bath and specializes in autonomous surface vessels and passive sonar.

Hugh Maclean Hugh Maclean is a Naval Architect whose experience ranges from large defense projects (for BMT Defence Services' Hydrodynamics Team) to high-speed tank testing of small interceptor or windfarm support vessels (at Seaspeed Marine Consulting) and taking a first prototype design through to production for long-endurance uncrewed surface vessels (at AutoNaut). Hugh has experience working in defense, marine research, offshore renewables and oil and gas – whether it is concept design and feasibility studies, unique data analysis to understand performance parameters of new technologies or managing a small specialist engineering and production team producing new customer vessels. He has a masters in Ship Science from Southampton University and has since worked as a specialist naval architect and managing a multidiscipline engineering team.

Jan Bujalka Jan Bujalka is an R&D Engineer working from First Idea to Product Handover, with experience in Designing Digital and Analogue electronic systems. He has an Ing. Master of Engineering degree in Automotive Electronics and has been working with Seiche Ltd. as an Embedded Software Engineer since 2016.

Jon Narramore Jon Narramore joined Seiche in 2012 and brought a wealth of Research and Development experience to the company. Responsible for several of the stand-alone deployment technologies now used by Seiche including the Modular Drift Buoys and the PAM-CAT Hydrophone Platforms. He led the redesign of the DTLA mechanical components and the Hydraq project. He is typically involved from conception through to deployment, including the integration of electronic data collection and transmission systems into the deliverable package. An experienced 3D CAD designer drawing on CNC machining experience, Jon works with the CAD-CAM-CNC approach taken at Seiche to produce manufacturable designs. This, combined with a practical system integration approach and being collaborative by nature, contributes to real-world solutions.

Ben Thomas Benjamin Thomas received the M.Eng. degree in engineering science from the University of Oxford, Oxford, U.K., in 2015 and the Ph.D. degree in the field of high-precision navigation and bathymetry estimation using interferometric synthetic aperture sonar from the University of Bath, Bath, U.K., in 2020. In 2017, he spent three months in La Spezia, Italy, as a Visiting Scientist with the NATO Centre for Maritime Research and Experimentation (CMRE), La Spezia, Italy. Since 2019, he has been a Research Associate with the University of Bath and specializes in the field of synthetic aperture sonar micronavigation.

Philippe Blondel Philippe Blondel received the DEUG-A degree in physics from the University of Rouen, France, in 1985, the Maîtrise degree in physics from the University of Paris-XI, France, in 1987, and the Ph.D. degree in physics and remote sensing from the University of Paris-VII, France, in 1992. He worked at the University of Washington on sonar imaging of mid-ocean ridges as a Lavoisier Fellow, carrying on this work as a NERC Fellow at the Institute of Oceanographic Sciences, Deacon Laboratory, and the Southampton Oceanography Centre (U.K.). He moved to the University of Bath, Bath, U.K., in 1999, where he is now Senior Lecturer in Physics and Director of the Centre for Space, Atmosphere, and Ocean Science. He has written several research textbooks including the Handbook of Sidescan Sonar (New York, NY, USA: Springer-Verlag, 2009) and Acoustic Investigation of Complex Seabeds (Springer Briefs in Oceanography, 2017). His research interests include acoustic imaging of marine habitats, underwater soundscapes and anthropogenic impacts, and acoustic monitoring of Arctic processes. He is a Fellow of the Institute of Acoustics and a Fellow of the Geological Society of London.

Alan Hunter Alan Hunter (Senior Member, IEEE) received the B.E. (Hons.) and Ph.D. degrees in electrical and electronic engineering from the University of Canterbury, Christchurch, New Zealand, in 2001 and 2006, respectively. From 2007 to 2010, he was a Research Associate with the University of Bristol, Bristol, U.K., and from 2010 to 2014, he was a Defense Scientist with TNO (Netherlands Organisation for Applied Scientific Research), Hague, The Netherlands. In 2014, he joined the Faculty of Engineering, University of Bath, Bath, U.K., where he is currently a Reader. Since 2017, he has been an Adjunct Associate Professor with the Department of Informatics, University of Oslo, Oslo, Norway. His research interests are in underwater acoustics, sonar imaging of the seafloor, and autonomous underwater systems. Dr. Hunter is an Associate Editor for IEEE Journal of Oceanic Engineering.